Atomic layer deposition and performance of ZrO_2-Al_2O_3 thin films

Kaupo Kukli,[a,b,*] Marianna Kemell,[a] Helena Castán,[c] Salvador Dueñas,[c] Helina Seemen,[b] Mihkel Rähn,[b] Joosep Link,[d] Raivo Stern,[d] Mikko J. Heikkilä,[a] Mikko Ritala,[a] Markku Leskelä[a]

[a]*Department of Chemistry, University of Helsinki, P. O. Box 55, FI-00014 Helsinki, Finland.*
[b]*Institute of Physics, University of Tartu, W. Ostwald 1, 50411 Tartu, Estonia.*
[c]*Department of Electronics, University of Valladolid. Paseo Belén, 15. 47011 Valladolid, Spain.*
[d]*National Institute of Chemical Physics and Biophysics, Akadeemia tee 23, 12618 Tallinn, Estonia.*
**Corresponding author. E-mails: kaupo.kukli@helsinki.fi, kaupo.kukli@ut.ee*

Abstract

Thin mixed and nanolaminate films of ZrO_2 and Al_2O_3 were grown by atomic layer deposition from the corresponding metal chlorides and water. The films were grown at 350 ^{o}C in order to ensure ZrO_2 crystallization in the as-deposited state. The relative thicknesses of layers in the structure of the nanolaminates were controlled in order to maximize the content of metastable polymorphs of ZrO_2 that have higher permittivity than that of the stable monoclinic ZrO_2. The multilayer films demonstrated interfacial charge polarization and saturative magnetization in external fields. The conductivity of the films could be switched between high and low resistance states by applying voltages of alternating polarity.

Introduction

ZrO_2 is a widely studied solid compound owing to its useful physical and chemical properties that are influenced also by its phase composition and structural ordering. ZrO_2 has monoclinic structure under normal conditions. ZrO_2 can also exist in the form of high-temperature tetragonal or cubic polymorphs, and also possess structures of brookite or cotunnite at high pressures.[1] The lattice of the brookite-type orthorhombic zirconia may herewith be regarded as the least determined one.[1] The cubic and tetragonal phases, metastable under normal conditions, possess higher relative dielectric permittivity than the monoclinic phase. Thus, phase-stabilized ZrO_2 has been explored and is exploited as high-permittivity dielectric materials in memory capacitors.[2] The orthorhombic phase of ZrO_2 has seldom been purposefully synthesized and studied, but has been proposed to possibly polarize nonlinearly and saturatively in external electric fields, similarly to the corresponding HfO_2 phase.[3]

Metastable zirconia phases can be formed either in the nanocrystalline form of ZrO_2, or after doping ZrO_2 with other metals or metal oxides. For example, tetragonal/cubic zirconia nanoparticles stabilized by doping with up to 50 mol % Al_2O_3 have been prepared by chemical vapor synthesis.[4]

ZrO_2 and Al_2O_3 based multilayer structures may effectively serve as memory capacitor dielectrics.[5-8] Al_2O_3 layers therewith serve as both stabilisers of the tetragonal zirconia and complementary internal barriers to leakage electron conduction. ZrO_2-Al_2O_3 laminates have also been considered as gas-diffusion barriers for encapsulation of organic electronics,[9,10] and charge carrier stopping layers in flash memory cell prototypes.[11] Besides applications in electronics, ZrO_2-Al_2O_3 mixtures and laminates have been evaluated as hard coatings deposited using either physical vapor deposition[12] or electrophoretic deposition technique.[13]

In earlier ALD processes of ZrO_2 and Al_2O_3, alternating saturative surface reactions between $ZrCl_4$ or $Al(CH_3)_3$ and H_2O at 300 °C were exploited.[5,14] Later, TiN–$ZrAl_xO_y$ –TiN MIM capacitors have been fabricated by ALD[6,8] with TiN electrodes formed by pulsed chemical vapor deposition using $TiCl_4$ and NH_3 as reactants. The nanolaminates of ZrO_2 and Al_2O_3 were grown by ALD, respectively, from $Zr[N(CH_3)C_2H_5]_4$-O_3 and $Al(CH_3)_3$-O_3 at 275 °C[6-8] or 80 °C.[9,10] ZrO_2–Al_2O_3 mixtures have been grown by ALD to investigate stable homogeneous amorphous structure as a high-k layer.[14] *In situ* high temperature X-ray diffraction tests have shown that the ZrO_2 mixed with 42-61 mol% Al_2O_3 started to crystallize at 900 °C, whereas non-mixed ZrO_2 was definitely crystallized already at about 500 °C. After rapid thermal annealing at 900 °C, the $ZrAl_xO_y$ film remained amorphous, whereas at 1000 °C tetragonal ZrO_2 was formed.[14]

This study was conducted in order to investigate the feasibility to grow by ALD such ZrO_2-based thin films, where the high-permittivity phases would dominate. This was attempted both by mixing and multilayering with Al_2O_3. The films were grown using metal chloride precursors at 350 °C. The temperature was chosen in order to reliably initiate crystal growth in 30-50 nm thick ZrO_2 films and, in the films grown at 350 °C, also the content of residual chlorine should not exceed 0.5 at.%.[15] The resulting dielectrics were evaluated in resistive

switching and internal charge polarization regimes. In addition, magnetization of the films was examined in vibrating sample mode in external field.

Experimental details

The films were grown in a commercial flow-type hot-wall reactor F120[16] (ASM Microchemistry, Ltd.) from $ZrCl_4$ (99.9 %, Aldrich), $AlCl_3$ (99%, Acros Organics) and H_2O. Growth temperature was held at 350 °C. $ZrCl_4$ and $AlCl_3$ were evaporated at 170 and 95 °C, respectively from open boats inside the reactor, and transported to the substrates by the N_2 flow. The pressure in the reactor chamber during the deposition process was below 10 mbar. The primary flows of carrier gas were kept at 400 sccm in the case of both metal precursor as well as water pulses. The consumption of H_2O was controlled by the needle valve and was approximately 2×10^{-5}g/cycle. [17]

The cycle times used were 0.5–0.5–0.5–0.5 s, denoting the sequence metal precursor pulse–purge–water pulse–purge. The substrates were 5 × 5 cm × cm pieces, cut out of undoped Si(100) covered with a 1.5–2.0 nm thick wet-chemically-grown SiO_2. In addition, also conducting substrates were used for the deposition of ZrO_2, based on (100) silicon with a resistivity of 0.014–0.020 Ω·cm, i.e., boron-doped to concentration up to $5 \times 10^{18} – 1 \times 10^{19}/cm^3$, and coated with 10 nm thick chemical vapor deposited titanium nitride layer. The films were grown to thicknesses ranging from ca. 5 to 100 nm. The thickest films were used for the conveniency of compositional measurements. The Al to Zr content was varied by changing the ratio of subsequent Al_2O_3 and ZrO_2 deposition cycles. The number of subsequent Al_2O_3 and ZrO_2 deposition cycles was varied separately in order to change the thicknesses of the constituent metal oxide layers. In this way, films of different artificial structures were deposited, ranging from ZrO_2 doped or mixed with low amounts of Al_2O_3 to Al_2O_3-ZrO_2 nanolaminates. The growth cycle sequences applied for the different samples are given in Table **I**.

PANalytical X'pert Pro MPD diffractometer was used to measure the grazing incidence X-ray diffraction patterns, while the incident beam angle was 1°. Magnetic measurements on selected samples were performed using vibrating sample magnetometer (VSM) option of the Physical Property Measurement System (PPMS) 14 T (Quantum Design), with the magnetic field parallel to the film surface. For electrical measurements, Al/Ti/ZrO_2/TiN/Si/Al capacitor

stacks were constructed with the effective capacitor area of 0.204 mm^2. Double-layer 110 nm/50 nm thick Al/Ti dot electrodes were evaporated through a shadow mask on the ZrO_2 films by electron beam evaporation, the Ti layer being in direct contact to ZrO_2. Backside ohmic contact was provided by evaporating 100–120 nm thick Al layer on HF-etched Si.

Table **I**. ZrO_2-Al_2O_3 cycle ratios, growth cycle sequences, film thicknesses, and cation ratios, measured by EDX

sample label	growth cycle sequences	d,nm EDX	Al:Zr EDX
120:6	$5 \times [120 \times ZrO_2 + 6 \times Al_2O_3] + 120 \times ZrO_2$	38	0.16
200:10	$3 \times [200 \times ZrO_2 + 10 \times Al_2O_3] + 200 \times ZrO_2$	44	0.24
100:1	$6 \times [100 \times ZrO_2 + 1 \times Al_2O_3] + 100 \times ZrO_2$	41	0.30
ZrO_2	$700 \times ZrO_2$ reference	45	

Energy dispersive X-ray spectrometry (EDX) was applied for the measurements of the aluminum to zirconium cation ratio, and also for the estimation of the film thicknesses, using a Hitachi S-4800 scanning electron microscope (SEM) equipped with an Oxford INCA 350 EDX spectrometer. The EDX spectra were measured at 30 keV. The beam current and spectrometer gain were determined from a calibration measurement under the same beam conditions. The film thicknesses and ratios of the different elements were calculated from the k ratios of Zr, Al, and Cl Kα X-ray lines measured with the calibrated beam. These calculations were done with a GMRFILM program.[18] Selected nanolaminates on Si substrate were investigated by scanning electron microscopy (SEM) using FEI Helios Nanolab™ 600 DualBeam™ microscope equipped with focused ion beam (FIB) module and Omniprobe model 100.7 in-situ nanomanipulator. High-resolution transmission electron microscopy (HRTEM) studies for the characterization of the cross-sections of the nanolaminate structures were carried out using FEI Titan Themis 200 instrument with a field emission gun operated at 200 kV. The FIB equipped with nanomanipulator was used for creating lamellae for TEM. Before the start of the FIB milling process, small (~ 20 x 1 μm) and thin (~1 μm) rectangular shaped C and Pt layers were deposited from their precursor compounds on top of the specimen using electron beam (for the first C and Pt layers) and ion beam (the last Pt layer) to protect the area of interest during the lamella fabrication process. This was followed by routine milling process for two openings with the cross depth up to 5-10 μm in the Pt-stripe area parallel with it and leaving a strip with width of 50-70 nm between them. Lamellae transportation and attachment to the lift-out type TEM grid, final thinning and polishing

process were completed. The Ga ion beam was used for milling, thinning and polishing, nanomanipulator for lamellae transportation and Pt deposition for lamellae attachment steps.

Results and discussion

Film composition and structure

The content of aluminum, as detected by EDX, was measurable and quantified, but not directly correlated to the ZrO_2:Al_2O_3 cycle ratio (Table **I**). The content of aluminum was evidently higher than expected, based on the knowledge on nominal growth rates or just cycle ratios of the constituent oxides. In the case of very few or just single monolayers of different compounds adsorbing on each other, certain intermixing of surface species and constituent atoms may take place,[19] additionally complicating the estimation of the maximum surface densities of metal atoms to be adsorbed during a single cycle. It is, however, known from earlier studies, that the atomic layer deposition of Al_2O_3 from $AlCl_3$ proceeds with average growth rate reaching 0.06 nm/cycle at 350 °C.[20,21] Taking this rate for a nominal constant value, only 0.36 and 0.60 nm thick uniform layers of Al_2O_3 should grow during every 6 and 10 ALD cycles, respectively. Quite similar growth rate, 0.05-0.06 nm/cycle, can be considered for ZrO_2 from $ZrCl_4$ and H_2O at 350 °C under similar conditions.[22] Taking into account the numbers of the growth cycles for constituent oxides applied, the Al:Zr atomic ratios should be as low as 0.042, 0.043 and 0.009 in the films grown using ZrO_2:Al_2O_3 cycle ratios 120:6, 200:10 and 100:1 (Table **I**), respectively. However, besides surface reactions between the alternately supplied precursors, one must consider also direct reactions between the earlier deposited oxide layer and the incoming precursor. In this regard, reaction between gaseous $AlCl_3$ and as-grown ZrO_2 can be written as follows:

$$1.5ZrO_2 + 2AlCl_3(g) = Al_2O_3 + 1.5ZrCl_4(g), \quad (1)$$

or, if the aluminum chloride exists, as often presumed, in dimeric form when evaporated:

$$1.5ZrO_2 + Al_2Cl_6(g) = Al_2O_3 + 1.5ZrCl_4(g). \quad (2)$$

Free energy (Gibbs energy) changes, ΔG, for the reactions (1) and (2) are -97 and -67 kJ/mol, respectively, at 350 °C.[23] The negative energies in both cases are indicative of highly spontaneous and likely reactions between bare zirconium oxide surface and adsorbing aluminum chloride, releasing volatile zirconium chloride. These reactions deposit additional

amounts of aluminum oxide constituting the growing solid layer, increasing the amount of aluminum oxide and, thus the Al:Zr cation ratio above that expected on the basis of growth rates and cycle ratios.

The nanolaminate films were deliberately grown as stacks consisting of alternate layers of distinct composition. One can see in the cross-section image (Fig. **1**) that the intermediate layers in laminates are nanocrystalline and not perfectly smooth – the crystallization obviously extends through neighbouring constituent layers. In addition to that, there are no sharp interfaces between the neighbouring layers (Fig. **1**, the second panel from top and bottom panel). In the case of smaller numbers of intermediate Al_2O_3 cycles, the separation of ZrO_2 layers by very thin Al_2O_3 layers is, visually, weakly recognized. If the material layer grows essentially polycrystalline, such as ZrO_2 in the present study, its surface can hardly be considered as atomically flat, despite the low layer thicknesses, but rather rough as typical for a polycrystalline material. Both direct exchange reactions (1) and (2) as well as developing roughness favor intermixing of the neighbouring atomic layers, which also leads to inhomogeneities and probably graded chemical composition. The successive layers of the constituent oxides may then not grow as perfectly superlattice-like structures, but somewhat irregular patterns of component layers without sharp interfaces between the neighbouring layers. The irregularities naturally increase with the decrease in the number of constituent oxide growth cycles, in our case most prominent for 1 and 6 Al_2O_3 cycles. The interfaces between the oxides are diffuse, although still weakly distinguishable due to their different chemical composition. The EDX profiling of Zr and Al metals throughout the films still allowed one to separate the Al_2O_3 and ZrO_2 constituent layers despite the very low thickness of Al_2O_3. In the case of the laminate built up on slightly thicker ZrO_2 and Al_2O_3 constituent layers, i.e. 10 Al_2O_3 cycles, the distinction between different constituent layers became more evident (Fig. **1**, the third panel from the top).

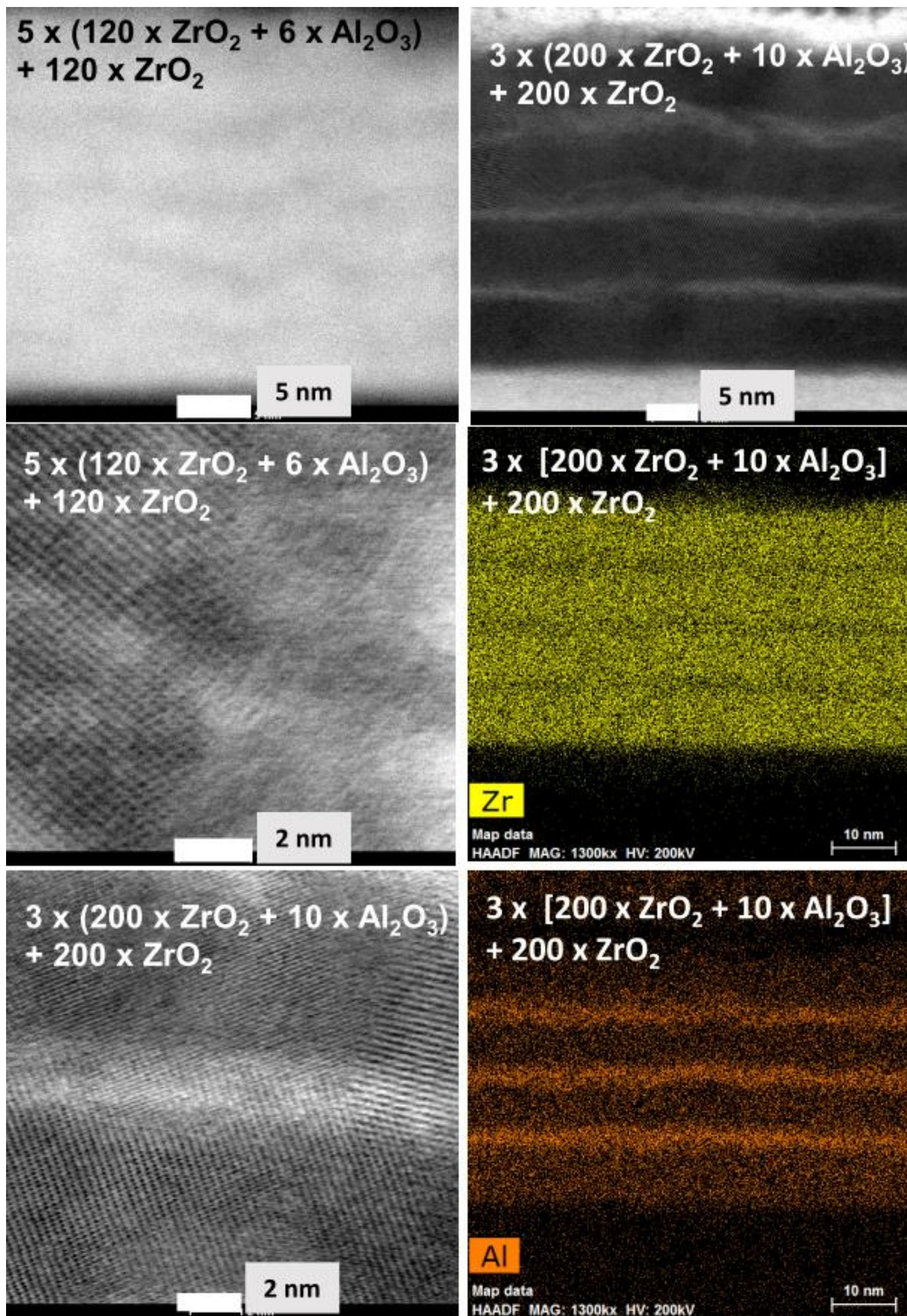

Figure 1. Cross-section HRTEM images of ZrO_2-Al_2O_3 nanolaminate structures with two different magnifications reflected by white scale bars. The second and third panels in the right column represent EDX profiles for Zr and Al, respectively. Growth cycle sequences are indicated by labels.

Figure 2 depicts bird-eye SEM images of ZrO_2 and ZrO_2-Al_2O_3 films. It is quite obvious that the surfaces of the films are in all cases uniformly covered by features which can plausibly be

related to the crystal growth and accompanying development of the grain size. One can see, that the ZrO_2 films not mixed with Al_2O_3 have, evidently, quite rough surface, as implied by the size of grains visible on the image (Fig. 2, top panel). The lateral grain size further decreases with the increase in the Al_2O_3 content.

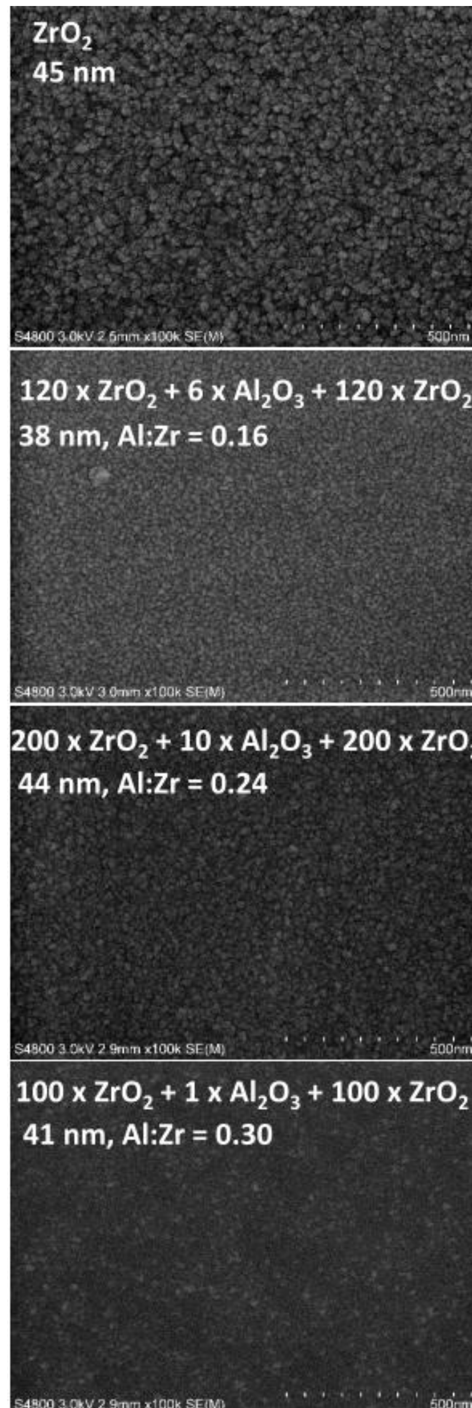

Figure 2. Bird-eye SEM images of a ZrO_2 reference film and ZrO_2-Al_2O_3 nanolaminate structures. The nanolaminate growth cycle sequences, total film thicknesses and cation ratios measured by EDX are indicated by labels. The growth cycle sequences are given for the last three constituent oxide layers terminating the multilayer structure.

Figure 3 represents X-ray diffraction patterns from a reference ZrO_2 film, and selected ZrO_2-Al_2O_3 nanolaminate structures deposited on SiO_2/Si and TiN/Si substrate surfaces. One can see that, actually in the 45 nm thick ZrO_2 film, not mixed with Al_2O_3 (Fig. 3, top panel) as well as in the ZrO_2:Al_2O_3, laminates and mixtures (Fig. 3, middle and bottom panels), the dominant phases were the metastable ZrO_2, i.e. either cubic or tetragonal polymorph. One could not exclude also the presence of orthorhombic ZrO_2. The locations of the diffraction peaks corresponding to the different phases are rather close to each other and the reflections are quite wide due to the nanocrystalline nature of the material, complicating unambiguous determination of the phase composition. At the same time, rather weak, but definitive reflections from the stable monoclinic ZrO_2 phase were recognized separately at 2θ values of 28.4^o and 31.2^o in the ZrO_2 film (Fig. 3, top panel), as parts of the nonsymmetric intense peak with center of gravity at 30.3^o in the nanolaminate with the thickest Al_2O_3 layers (Fig. 3, middle panel), as well as in the ZrO_2-Al_2O_3 nanolaminate with relatively low amounts of Al_2O_3 (Fig. 3, bottom panel). No significant differences in the phase composition of the ZrO_2 based films were observed on SiO_2/Si and TiN/Si substrates.

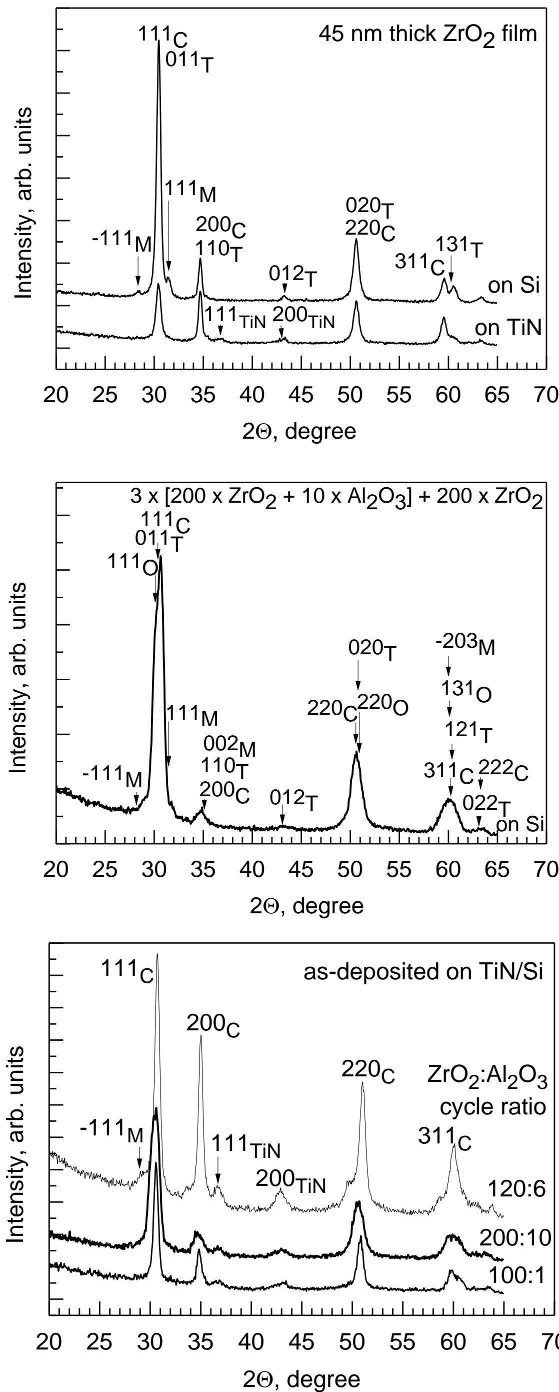

Fig. 3. GIXRD patterns of ZrO_2-Al_2O_3 nanolaminate structures as-deposited at 350 °C. The growth cycle sequences, substrates and Miller indexes are given by labels. The indexes are attributed to the reflections from ZrO_2 polymorphs denoted with subscripts M, O, C and T, corresponding, respectively, to monoclinic (PDF 037-1484), orthorhombic (PDF 037-1413), cubic (027-0997), and tetragonal (COD-210-0389) phases.

The crystallographic structure of the nanolaminates occurred stable against heat-treatment up to quite high-temperatures, approximately 1000 °C. Figure 4 depicts the results of high-temperature diffractometry which reveal the crystallization of ZrO_2-Al_2O_3 nanolaminate and mixture films upon annealing.

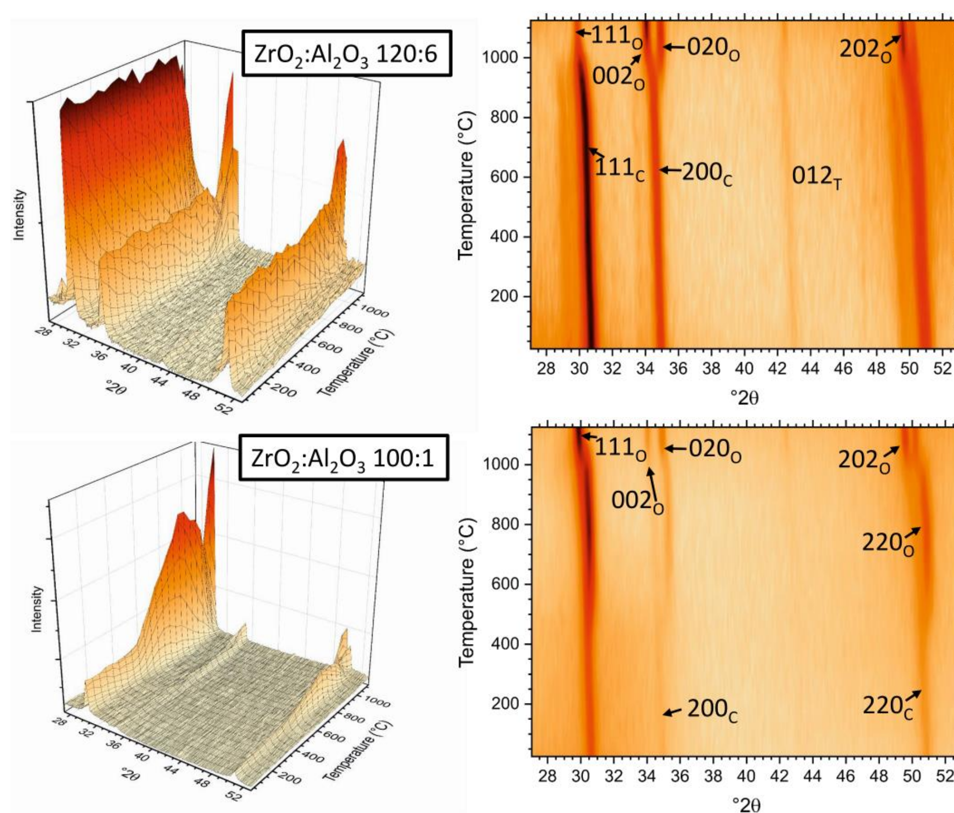

Fig. 4. High-temperature X-ray diffractograms in 3D (left column) and 2D (right column) formats from selected ZrO_2-Al_2O_3 films grown using ZrO_2:Al_2O_3 cycle ratios of 120:6 (upper row) and 100:1 (lower row). Relatively strong reflections from different phases are indicated by Miller indexes on 2D images, attributed to orthorhombic (O), cubic (C), and tetragonal (T) polymorphs of ZrO_2.

In the films grown with the ZrO_2:Al_2O_3 cycle ratios 100:1 an 120:6, one could initially, at room temperature and at moderately elevated temperatures (Fig. 4) detect strong diffraction peak at 30.48 2θ°, belonging to the 111 reflection of the cubic polymorph of ZrO_2 (Card 027-0997). Distinctive diffraction peaks of moderate intensities, attributed to the 200 and 220 reflections from the cubic phase, were observable at 35.17 2θ° and 50.64 2θ°, respectively. Weaker reflections at 43.1 and 50.4 2θ° may be assigned as those of 012 and 112 of the tetragonal ZrO_2 (COD card 210-0389).

Interestingly, the films initially formed with the cubic and/or tetragonal phase of ZrO_2, most probably, did not retain precisely the same phase composition, but the most prominent transformations took place at about 1000 ^oC, when the temperature was sequentially increased up to 1200 ^oC. The transition occurred between the cubic and tetragonal or, possibly, also the orthorhombic phases of ZrO_2. Quite distinctive diffraction peaks (Fig. 4) were recorded, while the most intense and also rather wide reflection at around 30.5^o sharpened and further intensified at 30.2^o. Besides cubic/tetragonal ZrO_2, this peak could be attributable to the 111 reflection of the orthorhombic phase of ZrO_2 (Card 037-1413). At higher angles, even more characteristic peaks could be detected at 34.2, 35.3, 49.8, 50.08, and 50.98 $2\theta^o$, may be attributed to the 002, 020, 022, 202, and 220 reflections of the orthorhombic ZrO_2, respectively. It is, however, to be noted, that the orthorhombic phase here is not convincingly determined and be considered as the major one contributing to the composition of the solid. The reflections in Fig. 4 are designated as those of orthorhombic phase for the sake of reader's conveniency and to separate them from the monoclinic reflections. Reflections from the tetragonal phase of ZrO_2 can be considered and become indexed as 002 and 110 at 34.2 and 35.3 $2\theta^o$, respectively.

It is worth noting, that the phase formed at 1000 ^oC and higher temperatures, was transformed to a mixture of other phases upon cooling the samples back to the room temperature (Fig. 5). In the cooled films grown with ZrO_2:Al_2O_3 cycle ratios 100:1 and 200:10, strong diffraction peaks were detected at 28.18^o and 31.5^o, unambigously attributed to the -111 and 111 reflections from the monoclinic ZrO_2 (card 037-1482). In the same samples, additional, but essentially weaker 200, 002, -112, 220 and 022 reflections from the monoclinic phase could be recognized (Fig. 5). At the same time, a strong peak apparent at 30.3-30.5^o was also retained, referring to the considerable contribution from either cubic or tetragonal polymorph of ZrO_2.

In the cooled film that was initially grown with the ZrO_2:Al_2O_3 cycle ratio 120:6, the otherwise major monoclinic -111 and 111 reflections did not appear at all, and the peak at 30.1-30.5^o, i.e. the one most characteristic of any metastable phases, was also of insignificantly low intensity. In the ranges of higher diffraction angles the peaks could be centered at 34.7^o, 35.4^o, 49.3^o and 50.1^o, possibly referring to 002 and 110 tetragonal, and 220 and 022 monoclinic reflections from ZrO_2, respectively.

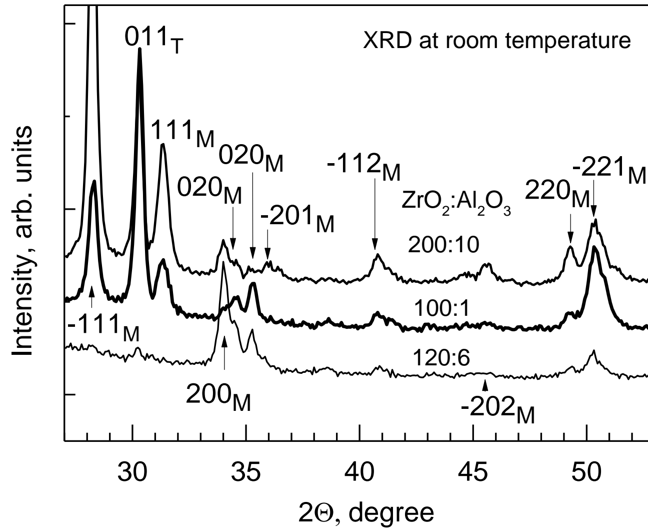

Fig. 5. X-ray diffractograms measured at room temperature after completion of the high-temperature X-ray diffractometry measurements (see Fig. 4) of the $ZrO_2:Al_2O_3$ films grown with cycle ratios indicated by labels. Also indicated are the Miller indexes assigned at the peaks. Subscripts T and M denote the cubic and monoclinic phases of ZrO_2.

In summary, the metastable phase composition of $ZrO_2:Al_2O_3$ nanolaminates and mixtures was sensitive to the aggressive annealing at high temperatures, reaching 1000-1200 °C. The degree of crystallization was evidently increased. Nonetheless, after cooling the films back to the room temperature, phase transition occurred, forming solid material with marked contribution from the stable crystallographic phase.

Electrical and magnetic behavior

Figure 6 represents charge polarization versus applied voltage loops from the ZrO_2 reference film and nanolaminates. The charge polarizing in the Al/Ti/ZrO_2-Al_2O_3/TiN/Si/Al stacks is likely due to the carrier transport between Ti and TiN electrodes. The charge may become trapped, likely, at interface barriers between the different metal oxide layers constituting the laminate structure, and, additionally, at the probably disordered interface between the zirconium oxide and titanium nitride electrode, enhancing interfacial polarization and causing

hysteretic behavior during backward sweep of the voltage. This is more prominent in the almost fully metastable nanolaminate films, compared to the ZrO_2 reference film. The charge polarization in the nanolaminate films is, obviously, dramatically higher compared to that recorded in the ZrO_2 film without Al_2O_3 intermediates (Figure **6**), referring to the role of the internal interfaces between the constituent oxide layers.

These charge-voltage loops, however, do not convincingly describe the behavior of ferroelectric material although certain contribution from remanent polarization could not be fully excluded. For instance, in the case of the orthorhombic phase of ZrO_2, stabilized in ALD-grown films, better defined ferroelectric-like hysteresis was observed.[24] For the films grown in the present study, saturation in polarization curves was not quite observed. In order to induce and record ferroelectric-type polarization in an oxide material, the film has to be initially formed as a well insulating dielectric solid, to avoid the interference from leakage currents enabling charge accumulation at oxide/electrode interfaces.

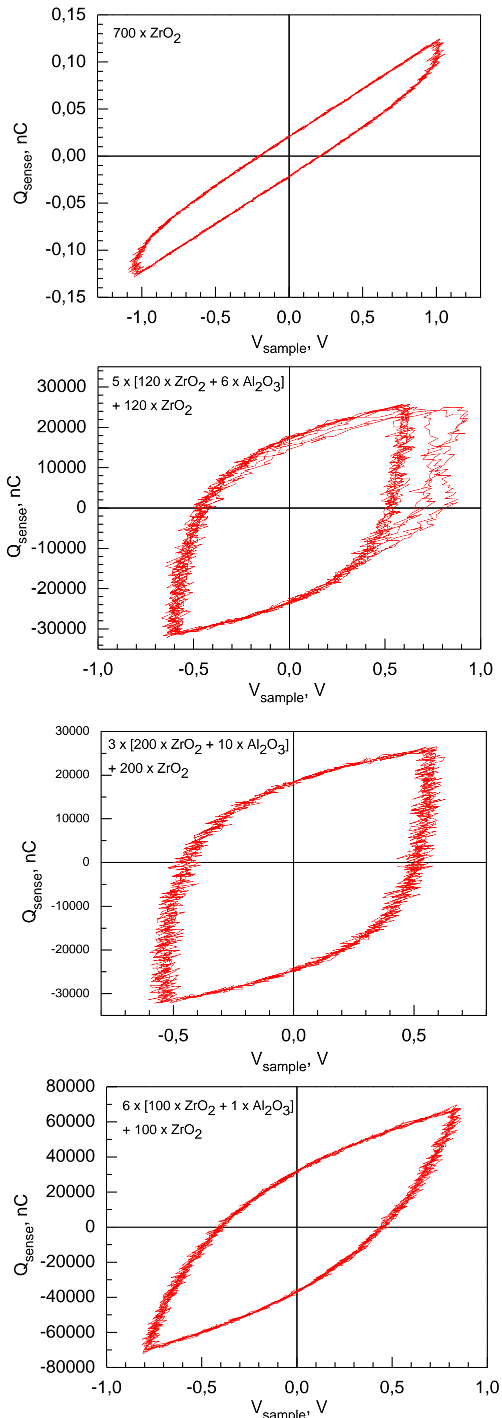

Figure 6. Charge polarization versus applied voltage behavior of reference film and nanolaminates. The ALD cycle sequences applied for the growth of oxide samples is given by labels.

All the samples examined in this study basically showed insulating behavior, but possessed considerably defective structure enabling switching between two states of different conductivity. After a forming voltage step, they behaved as elements with two clearly different memory states: high-resistance state (HRS) and low-resistance state (LRS). The forming cycle as an initial electrical stress necessary to activate the switching property consisted of DC bias ramp from 0 to 3-4 V, with a current compliance of 10 mA. In Figure 7, upper panel, the forming step and subsequent very first I-U memory cycles are depicted for the ZrO_2-based sample. One can see that the forming voltage is markedly higher compared to the further functional voltages in the resistive switching regime. The current-voltage behavior with characteristic consequentive loops in the resistive switching regime were highly repetitive with reproducible memory window between high and low resistance states. Comparison of the I-U loops of the films with different relative contents of Al_2O_3 is shown in Fig. 7, lower panel. The introduction of small amounts of Al_2O_3 extends the voltage range in which the loops appear, and provides narrower windows between the high and low resistance states. These particular results imply that the current window can be widened by increasing the Al:Zr ratio. Further, extended, studies would be required to optimize the aluminum content and relative thicknesses of constituent oxide layers, in order to establish the structural conditions for the maximized memory window ranges.

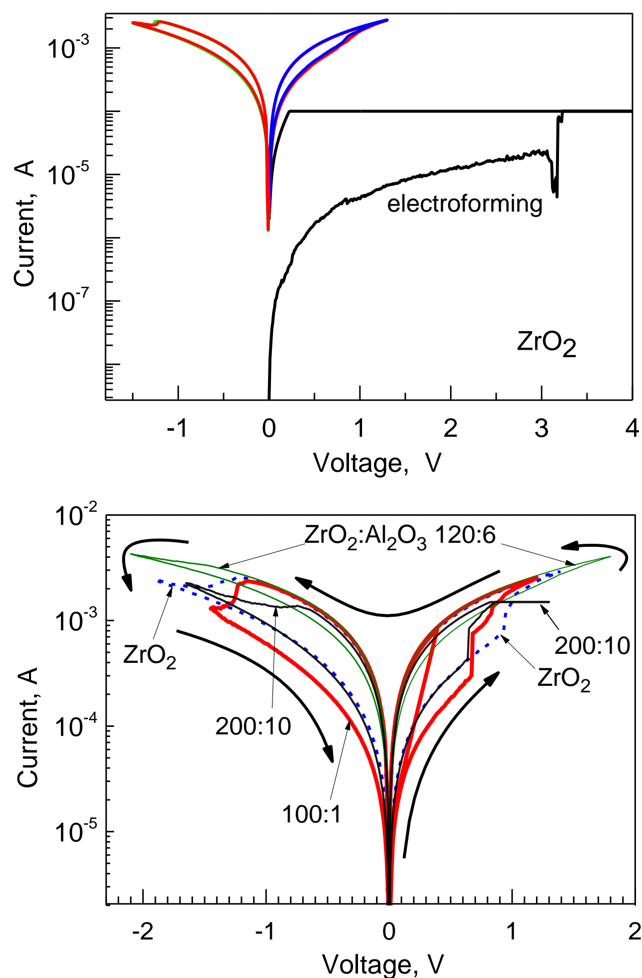

Fig. 7 Current *versus* voltage loops measured from ZrO_2 and ZrO_2-Al_2O_3 films. For ZrO_2, the first electroforming cycle is depicted (upper panel). Al:Zr atomic ratios and film thicknesses measured by EDX are given by labels (lower panel).

After the forming cycle, admittance parameters were recorded as well (Fig. 8). Both conductance and capacitance exhibited set and reset loops.[25] It is worth noting that, in the low resistance state of the ZrO_2 films, the capacitance and conductance signals were almost constant against voltage, which refers to the ohmic current behavior. It is also noteworthy that in the high resistance state, the linear dependences of capacitance and conductance on voltage were indicative of space charge limited current as the dominant conduction mechanism.

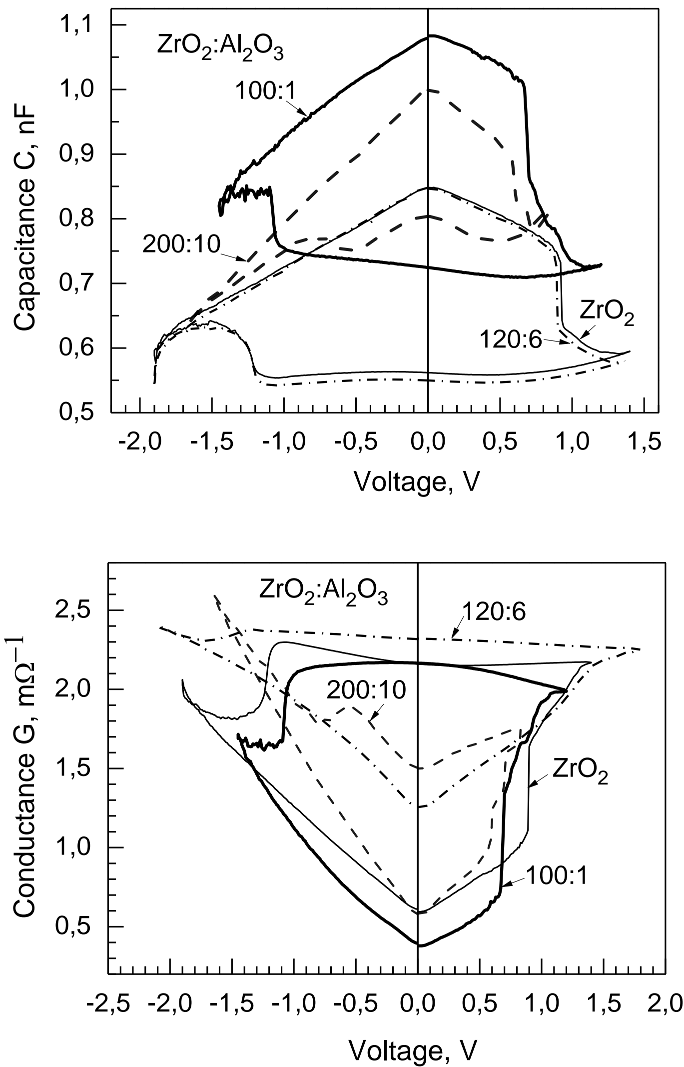

Fig. 8 Capacitance (upper panel) and conductance (lower panel) behaviors against bias voltage applied on Al/Ti/ZrO_2(:Al_2O_3)/TiN/Ti/Si/Al metal-insulator-metal type structures with constituent oxide cycle ratios indicated by labels. For detailed sample description, see Table **I**.

Capacitance and admittance parametrization completed the description of the hysteretic behavior of the layered materials. Thus, in order to more prominently demonstrate the difference between higher and lower resistance states in the materials deposited, voltage pulses with gradually increasing amplitude were applied on the Al/Ti/ZrO_2-Al_2O_3/TiN/Si/Al structures. In the sequence, after the pulse of variable voltage, bias was returned to 0.1 V and

the a.c. parameters were measured at this value. Hysteretic maps were recorded, representing both conductance and capacitance values measured at 0.1 V as functions of the programming voltage pulses previously applied in the sequence.[26] The resulting zero-bias admittance memory maps (Fig. 9) clearly demonstrated two different states, somewhat influenced by the dielectric composition. The memory reading process could in this case be carried out at 0 V, i.e. without power consumption. The memory window could, again, be modulated by changing the amount of Al_2O_3 in the laminates. The best power consumption behavior was achieved by samples grown with ZrO_2: Al_2O_3 cycle ratio of 100:1, where Al:Zr = 0.30, which possessed the lowest values of conductance in the high resistance state, and also the lowest values of SET and RESET voltages.

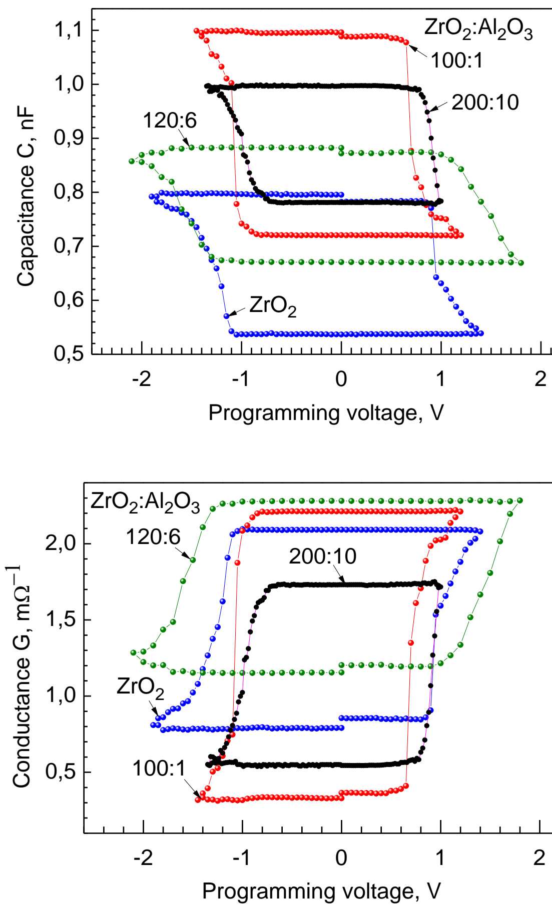

Fig. 9 Capacitance and admittance at 0.1 V bias against programming voltage for different samples indicated by labels (lower panel). For detailed sample description, see Table **I**.

Figure 10 demonstrates magnetization versus external magnetic field behavior of the ZrO_2-Al_2O_3 nanolaminate films grown on undoped diamagnetic silicon substrates.

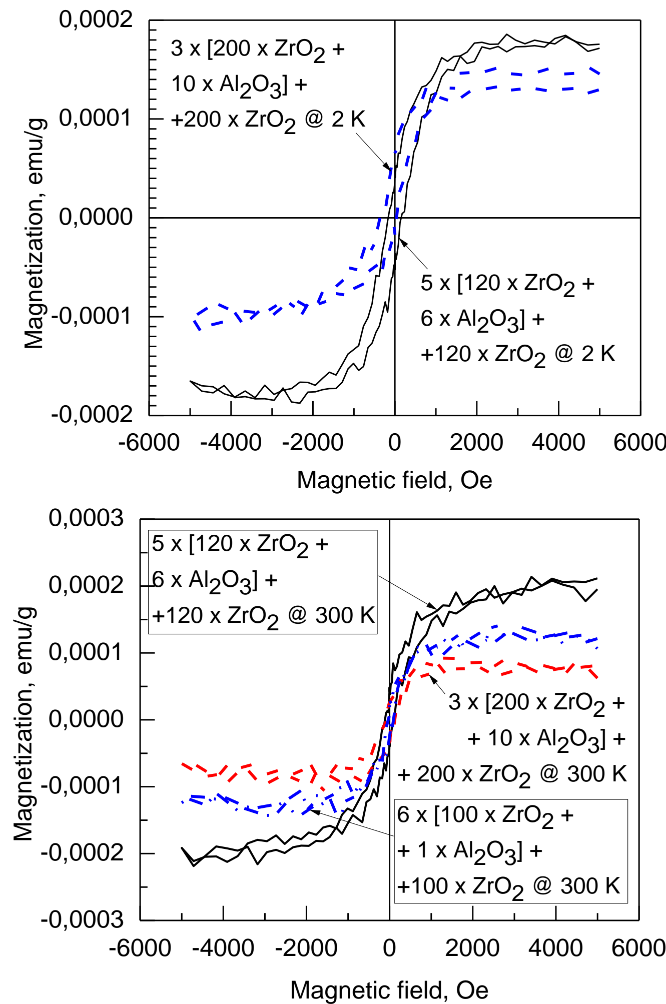

Figure 10. Magnetization-field loops for ZrO_2-Al_2O_3 nanolaminate films measured at 2 K (upper panel) and at room temperature (lower panel). The growth cycle sequences for nanolaminate oxide films are indicated by labels.

One can see in Fig. 10 that the magnetization in the ZrO_2-Al_2O_3 nanolaminates increased rapidly and nonlinearly with the external magnetic field strength before reaching saturation. Upon changing the field direction and strength, hysteresis loops were formed, demonstrating behavior generally characteristic of ferromagnetic material. No clear correlation between magnetization and content of aluminum in the ZrO_2 host material was recognized. Coercivity was higher at low measurement temperatures, i.e. at 2 K, reaching 200 Oe, compared to 40-70 Oe, recorded at room temperature. At the same time, no essential differences, measurable

within an order of magnitude, between saturation magnetizations at different temperatures were noticed.

The saturation magnetization, 1-2 × 10^{-4} emu/g, observed in this study is rather moderate. Also the coercive fields are close to those in soft ferromagnetic materials. It is noteworthy that these properties can be regarded as quite characteristic of undoped ZrO_2 or ZrO_2 containing nonmagnetic dopants. For comparison to literature data, Kumar and Ojha[27] have achieved saturation magnetization of 6.5 × 10^{-4} emu/g and coercive field 50-70 Oe in sol-gel synthesized ZrO_2 nanoparticles with size in the range of 8-23 nm, measured at room temperature. They have also observed, that mixing nanosized ZrO_2 with manganese suppressed the ferromagnetic-like performance and gave rise to paramagnetic behavior.[28] Ning *et al.*[29] have studied non-doped ZrO_2 films grown to thickness of 100 nm by electron beam evaporation and measured phase-sensitive saturation magnetization values of 0.69 and 0.04 emu/g in the films consisting of dominantly tetragonal and monoclinic polymorph of ZrO_2, respectively. In these films, however, the coercive field also did not exceed ca. 100 Oe. Further, it was found, that the ferromagnetism in zirconia-based films is driven by oxygen vacancies particularly characteristic of tetragonal phase of ZrO_2.[30] Somewhat higher saturation magnetization values could possibly be achieved in porous ZrO_2 films sputtered to anodic alumina substrates, with pore diameter of 5-45 nm, where the magnetization reached 119 emu/cm^3.[31] At the same time, coercive field remained at 100 Oe also in the latter study. Thus, the magnetization characteristics, recorded in the present study, generally remain in line with the earlier recent findings after measurements of ZrO_2-based thin solid structures.

Conclusions

Thin mixed and multilayered films of ZrO_2 and Al_2O_3 were grown by atomic layer deposition from $ZrCl_4$, $AlCl_3$ and H_2O. Application of growth cycles of alternate ZrO_2 and Al_2O_3 layers enabled formation of nanolaminates with variable aluminum content and metastable cubic and/or tetragonal polymorphs of ZrO_2 dominating the phase composition in the films. The content of aluminum in the films was somewhat increased likely due to the direct reactions between adsorbing aluminum chloride and underlying zirconium oxide. The films were grown at 350 °C, i.e. at temperature sufficiently high to ensure crystallization in the as-deposited state regardless of the constituent oxide cycle ratio. The multilayered films grown to the

thicknesses 40-50 nm demonstrated charge polarization, likely due to the effect of internal interfaces between constituent oxide layers, and clearly saturating magnetization in external fields, with recordable coercive field within several hundreds of oersteds. Resistive switching behavior was also recognized in the films, whereby the switching between high and low resistance states could be most reliably observed in ZrO_2:Al_2O_3 films with the highest amount of the aluminium oxide, i.e. with Al:Zr atomic ratio of 0.30. The films also demonstrated capacitance, conductance, and admittance hystereses against bias voltage, allowing one to recognize distinctive states of higher and lower conductivities. The width of the memory windows between the states was affected by the composition of the films, with the lowest admittance achieved in the films with Al:Zr atomic ratio of 0.30, implying the possibility to store information in such layers with minimized power consumption.

One could see that for the stabilization of the metastable ZrO_2 polymorphs, mixing or alternating layering of ZrO_2 with Al_2O_3 may not be ultimately needed, provided that the film thickness remains rather low within a few tens of nanometers, and high post-deposition annealing temperatures are not to be applied. However, combination of ZrO_2 with Al_2O_3 introduced useful artificial defects in the structure and resulted in significant changes in electrical properties. Charge polarization in aluminum zirconium oxide films increased dramatically, by several orders of magnitude compared to that in aluminum-free zirconium oxide. Also the difference between the high and low resistance states in the resistive switching regime exhibited larger window in the mixed and laminated films, compared to the bare binary ZrO_2.

Acknowledgements

The study was partially supported by the Finnish Centre of Excellence in Atomic Layer Deposition (284623), European Regional Development Fund project "Emerging orders in quantum and nano-materials" (TK134), Spanish Ministry of Economy and Competitiveness (TEC2014-52152-C3-3-R) with support of Feder funds, Estonian Academy of Sciences (SLTFYPROF), and Estonian Research Agency (IUT2-24, IUT23-7).

References:

1. R. Terki, G. Bertrand, H. Aourag, and C. Coddet, „Structural and electronic properties of zirconia phases: A FP-LAPW investigations," *Mater. Sci. Semicond. Proc*. **9**, 1006 (2006). http://dx.doi.org/10.1016/j.mssp.2006.10.033

2. B.-E. Park, I.-K. Oh, C. Mahata, C. W. Lee, D. Thompson, H.-B.-R. Lee, W. J. Maeng, and H. Kim, „Atomic layer deposition of Y-stabilized ZrO_2 for advanced DRAM capacitors," *J. Alloys Compd*. **722**, 307 (2017). http://dx.doi.org/10.1016/j.jallcom.2017.06.036

3. J. Müller, T. S. Böscke, U. Schröder, S. Mueller, D. Bräuhaus, U. Böttger, L. Frey, and T. Mikolajick, „Ferroelectricity in simple binary ZrO_2 and HfO_2," *Nano Lett.* **12**, 4318 (2012). http://dx.doi.org/10.1021/nl302049k

4. V. V. Srdić, and M Winterer, „Aluminum-doped zirconia nanopowders: Chemical vapor synthesis and structural analysis by Rietveld refinement of X-ray diffraction data," *Chem. Mater.* **15**, 2668 (2003). http://dx.doi.org/10.1021/cm021303q

5. W. F. A. Besling, E. Young, T. Conard, C. Zhao, R. Carter, W. Vandervorst, M. Caymax, S. De Gendt, M. Heyns, J. Maes, M. Tuominen, and S. Haukka, „Characterisation of ALCVD Al_2O_3 –ZrO_2 nanolaminates, link between electrical and structural properties," *J. Non-Cryst. Solids* **303**, 123 (2002). http://dx.doi.org/10.1016/S0022-3093(02)00969-9

6. D. Zhou, U. Schroeder, J. Xu, J. Heitmann, G. Jegert, W. Weinreich, M. Kerber, S. Knebel, E. Erben, and T. Mikolajick, „Reliability of Al_2O_3-doped ZrO_2 high-k dielectrics in three-dimensional stacked metal-insulator-metal capacitors," *J. Appl. Phys.* **108**, 124104 (2010). http://dx.doi.org/10.1063/1.3520666

7. D. Martin, M. Grube, W. Weinreich, J. Müller, W. M. Weber, U. Schröder, H. Riechert, and T. Mikolajick, „Mesoscopic analysis of leakage current suppression in $ZrO_2/Al_2O_3/ZrO_2$ nano-laminates," *J. Appl. Phys.* **113**, 194103 (2013). http://dx.doi.org/10.1063/1.4804670

8. S. Knebel, U. Schroeder, D. Zhou, T. Mikolajick, and G. Krautheim, „Conduction mechanisms and breakdown characteristics of Al_2O_3-doped ZrO_2 high-k dielectrics for three-dimensional stacked metal–insulator–metal capacitors," *IEEE Transact. Dev. Mater. Reliab.* **14**, 154 (2014). http://dx.doi.org/10.1109/TDMR.2012.2204058

9. J. Meyer, P. Görrn, F. Bertram, S. Hamwi, T. Winkler, H.-H. Johannes, T. Weimann, P. Hinze, T. Riedl, and W. Kowalsky, „Al_2O_3/ZrO_2 nanolaminates as ultrahigh gas-diffusion barriers—A strategy for reliable encapsulation of organic electronics," *Adv. Mater.* **21**, 1845 (2009). http://dx.doi.org/10.1002/adma.200803440

10. S.-W. Seo, E. Jung, H. Chae, and S. M. Cho, „Optimization of Al_2O_3/ZrO_2 nanolaminate structure for thin-film encapsulation of OLEDs," *Org. Electr.* **13**, 2436 (2012). http://dx.doi.org/10.1016/j.orgel.2012.07.007

11. M. S. Joo, S. R. Lee, H.-S. Yang, K. Hong, S.-A. Jang, J. Koo, J. Kim, S. Shin, M. Kim, S. Pyi, N. Kwak, and J. W. Kim, „Incorporation effect of thin Al_2O_3 layers on ZrO_2–Al_2O_3 nanolaminates in a composite oxide–high-oxide stack for floating-gate flash memory devices," *Jpn. J. Appl. Phys.* **46**, 2193 (2007). http://dx.doi.org/10.1143/JJAP.46.2193

12. A. Portinha, V. Teixeira, T. J. O. Carneiro, S. N. Dub, R. Shmegera, and C. J. Tavares, „Hard ZrO_2/Al_2O_3 nanolaminated PVD coatings evaluated by nanoindentation," *Surf. Coat. Technol.* **200**, 765 (2005). http://dx.doi.org/10.1016/j.surfcoat.2005.02.021

13. Z. Chlup, H. Hadraba, L. Slabáková, D. Drdlík, and I. Dlouhý, „Fracture behaviour of alumina and zirconia thin layered laminate," *J. Eur. Ceram. Soc.* **32**, 2057 (2012). http://dx.doi.org/10.1016/j.jeurceramsoc.2011.09.006

14. C. Zhao, O. Richard, E. Young, H. Bender, G. Roebben, S. Haukka, S. De Gendt, M. Houssa, R. Carter, W. Tsai, O. Van Der Biest, and M. Heyns, „Thermostability of amorphous zirconium aluminate high-k layers," *J. Non-Cryst. Solids* **303**, 144 (2002). https://doi.org/10.1016/S0022-3093(02)00977-8

15. K. Kukli, M. Ritala, J. Aarik, T. Uustare, and M. Leskelä, „Influence of growth temperature on properties of zirconium dioxide films grown by atomic layer deposition," *J. Appl. Phys.* **92**, 1833 (2002). http://dx.doi.org/10.1063/1.1493657

16. T. Suntola, Atomic layer epitaxy, *Thin Solid Films*, **216**, 84 (1992). http://dx.doi.org/10.1016/0040-6090(92)90874-B

17. R. Matero, A. Rahtu, M. Ritala, M. Leskelä, T. Sajavaara, Effect of water dose on the atomic layer deposition rate of oxide thin films, *Thin Solid Films* **368**, 1 (2000). http://dx.doi.org/10.1016/S0040-6090(00)00890-7

18. Waldo, R. A. Microbeam Analysis (San Francisco Press, San Francisco, CA, 1988), p. 310.

19. C. W. Wiegand, R. Faust, A. Meinhardt, R. H. Blick, R. Zierold, and K. Nielsch, „Understanding the growth mechanisms of multilayered systems in atomic layer deposition process," *Chem. Mater.* (2018). http://doi.org/10.1021/acs.chemmater.7b05128

20. S. J. Yun, J. S. Kang, M. C. Paek, and K.-S. Nam, „Large-area atomic layer deposition and characterization of Al_2O_3 film grown using $AlCl_3$ and H_2O," *J. Korean Phys. Soc.* **33**, S170 (1998).

21. L.Hiltunen, H. Kattelus, M. Leskelä, M. Mäkelä, L. Niinistö, E. Nykänen, P. Soininen, and M. Tiitta, „Growth and characterization of aluminium oxide thin films deposited from various source materials by atomic layer epitaxy and chemical vapor deposition processes," *Mater. Chem. Phys.* **28**, 379 (1991). http://doi.org/10.1016/0254-0584(91)90073-4

22. A. Tamm, M. Heikkilä, M. Kemell, J. Kozlova, K. Kukli, V. Sammelselg, M. Ritala, and M. Leskelä, „Atomic layer deposition and characterization of zirconium oxide–erbium oxide nanolaminates," *Thin Solid Films* **519**, 666 (2010). http://dx.doi.org/10.1016/j.tsf.2010.08.111

23. Outokumpu HSC Chemistry for Windows. program package, Version I. 10. Outokumpu Research OY, Pori, Finland (1993).

24. B.-T. Lin, Y.-W. Lu, J. Shieh, and M.-J. Chen, „Induction of ferroelectricity in nanoscale ZrO_2 thin films on Pt electrode without post-annealing," *J. Eur. Ceram. Soc.* **37**, 1135 (2017). http://dx.doi.org/10.1016/j.jeurceramsoc.2016.10.028

25. S. Dueñas, H. Castán, H. García, E. Miranda, M. B. Gonzalez, and F. Campabadal, „Study of the admittance hysteresis cycles in TiN/Ti/HfO_2/W-based RRAM devices," *Microel. Eng.* **178**, 30 (2017). http://dx.doi.org/10.1016/j.mee.2017.04.020

26. S. Dueñas, H. Castán, H. García, O. G. Ossorio, L. A. Domínguez, and E. Miranda, „Experimental observation of negative susceptance in HfO_2-based RRAM devices," *IEEE Electron Dev. Lett.* **38**, 1216 (2017). http://dx.doi.org/10.1109/LED.2017.2723054

27. S. Kumar, and A. K. Ojha, "Oxygen vacancy induced photoluminescence properties and enhanced photocatalytic activity of ferromagnetic ZrO_2 nanostructures on methylene blue dye under ultra-violet radiation," *J. Alloys Compd*. **644**, 654 (2015). http://dx.doi.org/10.1016/j.jallcom.2015.04.183

28. S. Kumar, S. Bhunia, and A. K. Ojha, "Experimental and theoretical evidence for the presence of room temperature ferromagnetism in undoped and Mn doped tetragonal ZrO_2 nanostructures," *Chem. Phys. Lett.* **644**, 271 (2016). http://dx.doi.org/10.1016/j.cplett.2015.12.026

29. S. Ning, P. Zhan, Q. Xie, Z. Li, and Z. Zhang, "Room-temperature ferromagnetism in un-doped ZrO_2 thin films," *J. Phys. D: Appl. Phys.* **46**, 445004 (2013). http://dx.doi.org/10.1088/0022-3727/46/44/445004

30. S. Ning, and Z. Zhang, "Phase-dependent and defect-driven d^0 ferromagnetism in undoped ZrO_2 thin films," *RSC Adv.* **5**, 3636 (2015). http://dx.doi.org/10.1039/c4ra11924j

31. R. Han, L. Qi, L. Liu, Q. Xu, G.-X. Guo, and H. Sun, "Microstructures and room temperature ferromagnetism of ordered porous ZrO_2 thin films sputter deposited onto porous anodic alumina substrates," *J. Magn. Magn. Mater.* **428**, 99 (2017). http://dx.doi.org/10.1016/j.jmmm.2016.12.034